CHEMISTRY OF MATERIALS

Article

pubs.acs.org/cm

Silicon/Hollow γ-Fe_2O_3 Nanoparticles as Efficient Anodes for Li-Ion Batteries

Gal Grinbom,[†] David Duveau,[‡] Gregory Gershinsky,[†] Laure Monconduit,[‡] and David Zitoun*[,†]

[†]Department of Chemistry, Bar Ilan Institute of Nanotechnology and Advanced Materials (BINA), Ramat Gan 52900, Israel

[‡]Institut Charles Gerhardt UMR CNRS 5253, ALISTORE European Research Institute (3104 CNRS) – AIME, Université Montpellier 2, CC1502, place E. Bataillon, 34095 Montpellier cedex 5, France

Supporting Information

ABSTRACT: Nanomaterials have triggered a lot of attention as potential triggers for a technological breakthrough in Energy Storage Devices and specifically Li-ion batteries. Herein, we report the original synthesis of well-defined silicon/iron oxide nanoparticles and its application as anode materials for Li-ion batteries. This model compound is based on earth abundant elements and allows for a full investigation of the electrochemical reactions through its iron oxide magnetic phase. The elaboration of silicon with iron oxide grown on its surface has been achieved by reacting an organometallic precursor $Fe(CO)_5$ with Si nanopowder and subsequent slow oxidation step in air yields hollow γ-Fe_2O_3 on the Si surface. This specific morphology results in an enhancement of the specific capacity from 2000 mAh/g_{Si} up to 2600 mAh/g_{Si}. Such a high specific capacity is achieved only for hollow γ-Fe_2O_3 and demonstrates a novel approach toward the modification of electrode materials with an earth abundant transition metal like iron. This result further emphasizes the need for precisely designed nanoparticles in achieving significant progress in energy storage.

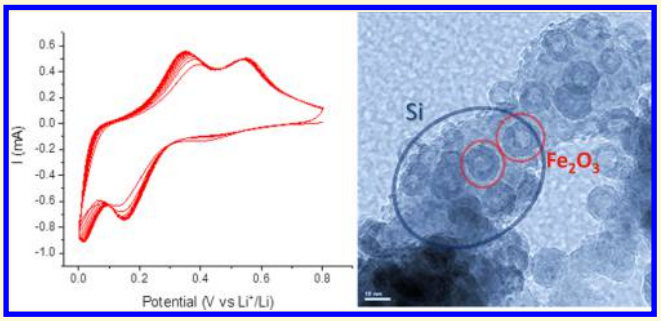

INTRODUCTION

The rechargeable Li-ion batteries (LIBs) display high energy density, which makes them the preferred energy storage device for portable applications. Si-based materials have the potential of serving as high energy density anodes through an alloying mechanism. Elemental Si shows a theoretical specific capacity of 3600 mAh/g for $Li_{15}Si_4$ alloy (10 times higher than commercial graphite anodes) and safe anodic behaviors. A stable silicon-based anode having an adequate number of charge/discharge cycles will ensure a faster transition to gasoline-free transportation. Nevertheless, the observed capacity fading continues to be the major drawback in silicon anodes. It has been attributed to the lattice cell expansion of silicon upon lithium uptake, resulting in the failure of stable solid electrolyte interphase (SEI) and loss of electrical intergrain contacts on charge. For solving this issue, several routes have been explored which include the use of amorphous or nanostructured silicon thin film,[1] silicon nanowires,[2,3] and very generally any nanostructured silicon material.[4]

In fact, the capacity fading has been attributed to a conjunction of several phenomena: mechanical constraints in the composite film due to Si expansion upon lithiation and side reactions with the electrolyte at the very reactive Si surface. The constant degradation of SEI on silicon[5] has led to the investigation of new electrolytes and specific coatings, which provide routes to passivate the surface.[6] Hundreds of cycles with high Coulombic efficiency can be achieved with a specific solvent, like fluoroethylene carbonate (FEC),[7] and charge limited procedure.[8,9]

Using silicon, an earth abundant material in Li-ion batteries, is very appealing and raises the question of purity needed to achieve a good anodic material. Indeed, mixed oxides/hydroxide of silicon and iron are the most abundant source for silicon, as a compound of general formula $Fe_xSi_yO_z$ (for instance Greenalite Fe_2-$3Si_2O_5(OH)_4$), with varying ratios of elemental silicon and iron. These minerals are the starting materials of about 80% of the world's production of elemental silicon. The metallurgical grade silicon consists of 96%–99% weight of silicon with metallic (mainly Fe) impurities.[10] Metallurgical grade silicon with around 5000 ppm of iron has been recently used as starting material for nanotextured Si anode.[11] The use of Si with Fe impurities poses several questions about the exact nature of Fe compounds in the pristine material, as well as during the battery lifetime, the role of Fe during the electrochemical cycle, and the stability of silicon SEI. Finally, any metallic impurity or alloy formed could also lessen the structure damage during the battery cycling as observed for other conversion materials.

On the other hand, iron is one of the most abundant elements in cathode materials (like in olivine $LiFePO_4$),[12,13] and the diffusion process of transition metals through the separator can occur during cycling, resulting in the contamination of the anode

Received: February 25, 2015
Revised: March 7, 2015
Published: March 10, 2015

DOI: 10.1021/acs.chemmater.5b00730
Chem. Mater. 2015, 27, 2703–2710

material. A pertinent investigation of the influence of transition metals in soon to be standard anode materials (silicon) seems worthwhile and timely. Moreover, iron displays a high magnetic moment, and the magnetic properties are highly sensitive to its oxidation state which is a good way to follow their oxidation states changes upon cycling.[14] γ-Fe_2O_3 is also known as an anode material.[15,16] According to Larcher et al.,[16] Fe_2O_3 nanoparticles insert lithium ions by forming a hexagonal $LiFe_2O_3$ phase. A phase transformation from a phase with a close-packed hexagonal anion lattice of $LiFe_2O_3$ to a disordered cubic structure of $Li_2Fe_2O_3$ occurs upon further lithiation. However, another study shows that Fe_2O_3 is converted to metallic Fe(0) nanoparticles (NPs) in a Li_2O matrix, which forms simultaneously during discharge.[17]

In this paper, we will report on the synthesis of anode nanomaterial made of hollow Fe_2O_3 specifically grown on the surface of the Si NPs and which show enhanced performance as an electrode in Li-ion batteries. A slow oxidation yields hollow Fe_2O_3 particles, which contributes to the high capacity of the anode. The observed enhancement is specific to hollow Fe_2O_3. The nanocomposite is fully characterized as a pristine material by High-Resolution transmission electron microscopy (HR-TEM), X-ray photoelectron spectroscopy (XPS), Mössbauer and magnetic measurements, and after cycling by magnetic measurements.

SYNTHESIS AND CHARACTERIZATION

Si/iron oxide nanostructures were synthesized by sequential organometallic decomposition of iron pentacarbonyl $Fe(CO)_5$ on Si nanostructures followed by oxidative or reductive treatments. The following samples were fully characterized by transmission electron microscopy (TEM), X-ray Diffraction (XRD), XPS, and superconducting quantum interference device (SQUID) magnetometer and tested as anode materials for Li-ion batteries. The starting material, Si nanopowder, commonly used in Li-ion battery research, is considered as standard anode material.[18] The Si nanostructured powder forms a network of nanocrystalline Si interconnected particles (Figure S1A) with a cubic crystallographic structure ($Fd\bar{3}m$, a = 5.4309 Å, JPCDS 27-1402) as shown from Selected Area Electron Diffraction (SAED) and XRD (Figure S1B). The reaction with $Fe(CO)_5$ yields pristine silicon−iron Sample 1, while oxidation in air yields Sample 2 and reduction in forming gas yields Sample 3 (Figure 1A). The reaction is quantitative and the stoichiometry Si/Fe, checked by induced coupled plasma atomic emission spectroscopy (ICP-AES), has been set to Si/Fe 4:1. Several atomic ratios (Si/Fe 6:1 and Si/Fe 100:1) were synthesized by the same reaction, Figure S2, but we are focusing on the 4:1 atomic ratio in this study.

The reaction with $Fe(CO)_5$ yields Sample 1 where TEM shows the nucleation of spherical particles of diameter 12 ± 3 nm specifically on the surface of Si (Figure 1B). The TEM shows the formation of nanoparticles of Fe on Si networks without any self-nucleation of Fe, following the schema on Figure 1A. A higher magnification TEM demonstrates the core/shell structure of the newly formed nanoparticles of iron (Figure 2A). Each particle consists of a core (dark) and a shell (bright) of about 2−3 nm thickness in the bright field TEM images. The network of Si remains crystalline, while the newly formed nanoparticles of iron are amorphous from HR-TEM study (Figure 2D). XRD of the samples is typical of nanocrystalline Si without any new crystalline phase formed during the reaction (Figure S1B).

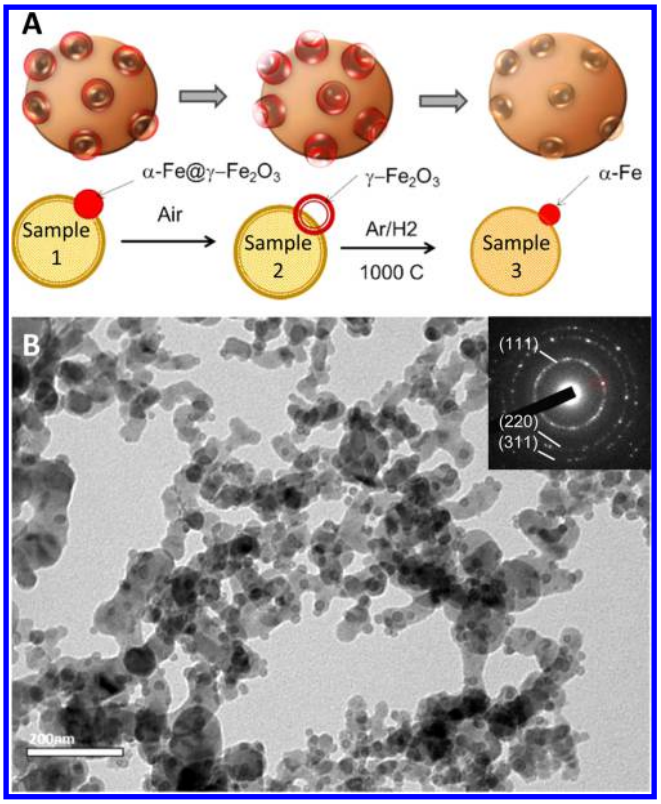

Figure 1. Schema of the synthetic process toward Si/Fe composite (A) and TEM image of Si/Fe composite (Sample 1) (B).

The exposure to air for several weeks fully oxidizes the Fe core and yields a shell of iron oxide with a single hole in the middle in Sample 2 (Figure 2B-D). The particles are homogeneous in size with an outer diameter of 13 ± 3 nm and an apparent thickness of the walls of 4 ± 2 nm. After annealing in forming gas, Sample 3 consists of iron NPs of 11 nm formed on top of the Si network (Figure 2C).

The newly formed NPs on the nanocrystalline Si are amorphous both from X-ray and electron diffraction studies. We used element sensitive techniques to characterize the nanocomposite. Transmission electron microscopy with electron dispersive X-ray spectroscopy (EDS) was used to map the elemental composition at the nanoscale for Sample 3 (Figure 3A-B). The TEM image is displayed in bright field and colored according to the EDS mapping. Elemental Fe (pink) is only located on the surface of silicon (yellow), and no diffusion of Fe in Si was detected at the level of precision of EDS. Similar work has been performed on Samples 1 and 2, which shows the distribution of Fe on the newly formed particles. EDS results are reported on Figure S3. Sample 3 is particularly interesting since the diffusion of Fe is a relevant point mainly for a high temperature processed sample, annealed at 1000 °C. Oxygen mapping shows the formation of an oxide layer which follows the surface of Si and Fe nanoparticles (Figure 3C).

X-ray Photoelectron Spectroscopy (XPS) shows the presence of Fe(III) or Fe(II) for Si/hollow NPs Sample 2, and the XPS could eventually correspond to Fe(II) species which can hardly be differentiated in terms of energy (Figure 3D). XPS shows the presence of two different species Fe(III)/Fe(II) and Fe(0) for the pristine Si/Fe Sample 1. After annealing to Sample 3, the ratio between the two different species turns in favor of the Fe(0) with a noticeable peak at 706 eV.

DOI: 10.1021/acs.chemmater.5b00730
Chem. Mater. 2015, 27, 2703−2710

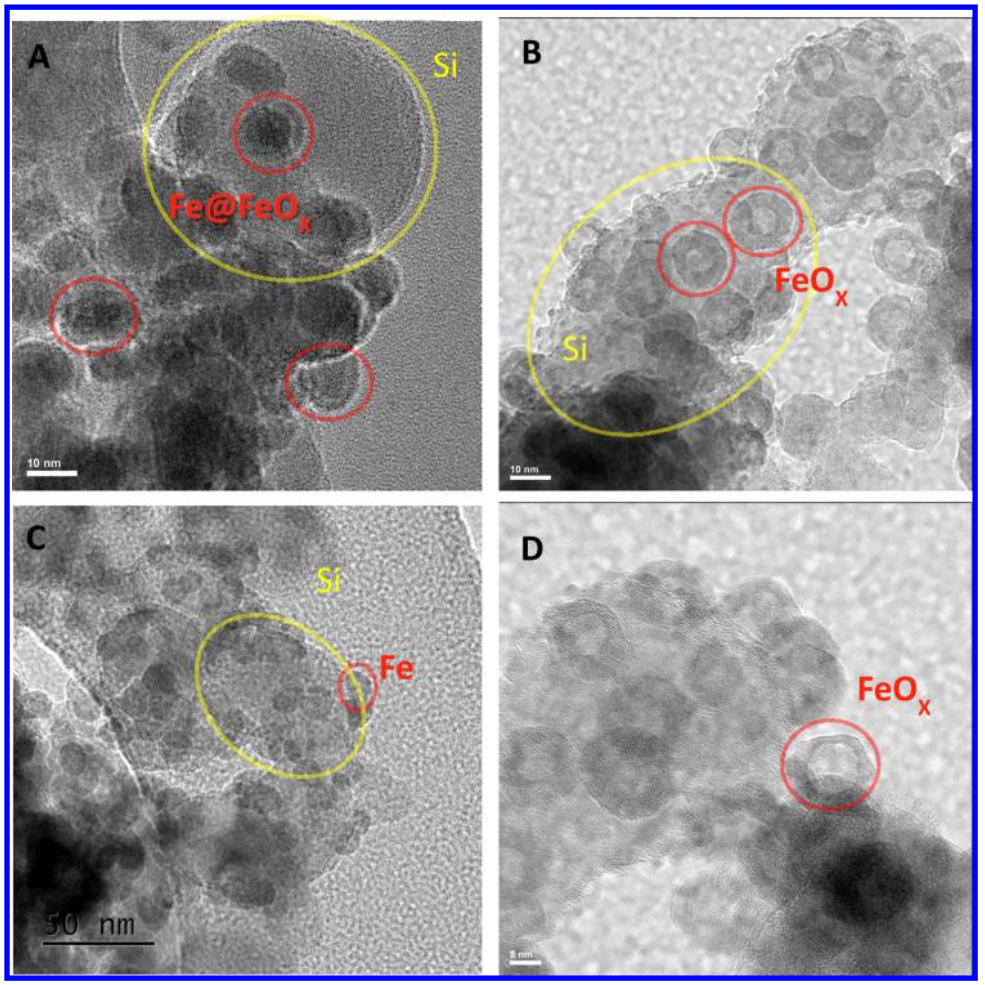

Figure 2. TEM image of Sample 1 (A), Sample 2 (B), and Sample 3 (C) and HR-TEM of sample 2 (D).

The samples display ferromagnetic behavior at room temperature (Figure 4A-B). The hysteresis loop was also measured at low temperature (T = 2 K), and the magnetic moment was normalized to the amount of Fe inferred from ICP-AES measurements. The lack of complete saturation is well documented as a surface effect of magnetically ordered oxides where the spins are canted in a "hedgehog" configuration. Obviously, the two Samples with the more extended surface area (hollow and core/shell) are more sensitive to this effect. The pristine Si/Fe (Sample 1) reaches a magnetic moment of 73 emu/g_{Fe} (or 73 A·m^2/kg_{Fe}). The Si/hollow iron oxide (Sample 2) displays a magnetic moment of 67 emu/g_{Fe}, while the Si/Fe annealed (Sample 3) reaches the value of 136 emu/g_{Fe}. The square hysteresis loops are typical of a ferro- or ferrimagnetic behavior with a coercive field highlighted on the inset (Figure 4A). The values of the magnetization can be compared with bulk values for bcc Fe (220 emu/g_{Fe}), maghemite γ-Fe_2O_3 (80 emu/g_{Fe}), and inversed cubic spinel ferrite Fe_3O_4 (92 emu/g_{Fe}), which are the main ferro- or ferrimagnetic phases. The magnetic moment measured on the annealed Sample 3 was far above the values of iron oxides which indicates the presence of metallic Fe in the composite. The pristine Sample 1 and Sample 2 after oxidation approached the value of maghemite γ-Fe_2O_3 even if the presence of Fe or Fe_3O_4 cannot be excluded. The values of the coercive fields are also consistent with the presence of mainly γ-Fe_2O_3 in Sample 2 (H_C = 100 mT) and mainly Fe in Sample 3 (H_C = 33 mT), while pristine Sample 1 would include the two phases. The hysteresis loop of Sample 2 (hollow particles) was asymmetric due to large magnetic hysteresis as already reported for nonsupported γ-Fe_2O_3 hollow nanoparticles.[19]

Temperature dependent measurement at low field (5.0 mT) shows a blocking temperature higher than 300 K for the three samples, consistent with the existence of a ferromagnetic phase and the particle size (>11 nm) obtained for the three samples (Figure 4B). The M-T curves do not show any paramagnetic phase as evidenced by the low temperature behavior of the FC.

The Mössbauer spectrometry of Sample 2 Si/hollow Fe_2O_3 nanocomposites at T = 4.2 K is shown in Figure 5A, and the magnetic hyperfine field is given in Figure 5B. The spectrum can be entirely fitted with a sextuplet centered on the isomer shift of 0.50 mm/s, which relates to the magnetic order of Fe(III) atoms. Fe_2O_3 can crystallize within two phases: maghemite or hematite. The maximum of the magnetic hyperfine field (50 T) is lower than reported for hematite (54 T). Moreover, hematite has a significant quadrupole shift which is not the case of this sample. The sample is a distribution of maghemite γ-Fe_2O_3 hollow NPs.

The formation of hollow γ-Fe_2O_3 has been reported in the literature, and, more generally, formation of high valence metal oxide can derive from the slow oxidation of either corresponding metallic or low oxidation metal oxide.[20] The specific morphology has been attributed to the Kirkendall effect which results from the higher diffusion rate of metallic cation (Fe^{3+}) compared to the chalcogenide (O^{2-}). The kinetics of the oxidation process have

DOI: 10.1021/acs.chemmater.5b00730
Chem. Mater. 2015, 27, 2703−2710

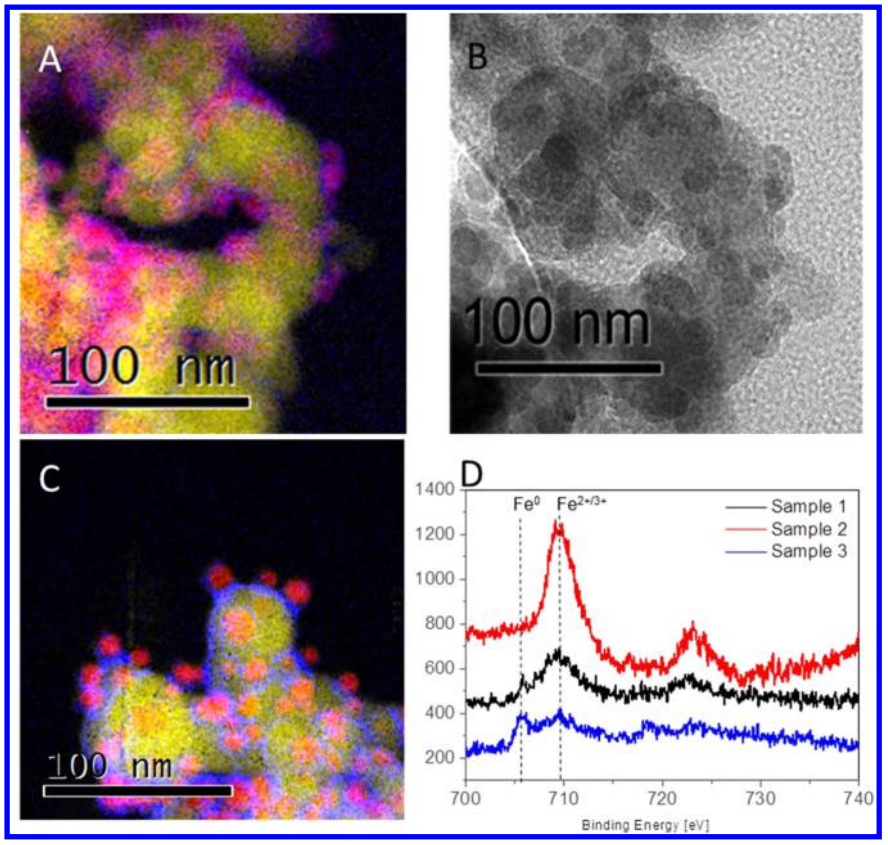

Figure 3. EDS mapping of Sample 3 Si/Fe NCs (Si: yellow, Fe: pink, O: blue) (A,C); corresponding HR-TEM image (B); X-ray Photoelectron Spectroscopy (XPS) of Sample 1 Fe@Fe_2O_3/Si NCs (black), Sample 2 hollow Fe_2O_3/Si NCs (red), Sample 3 Fe/Si NCs (blue) (D).

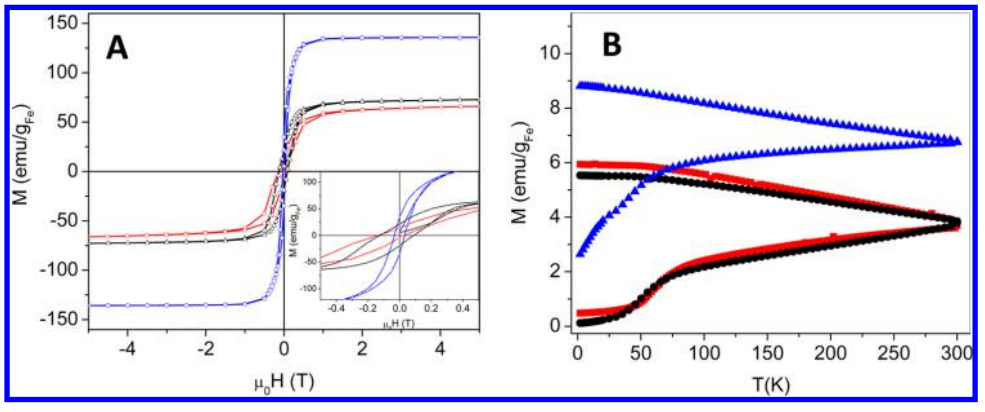

Figure 4. SQUID measurements of Si/Fe@Fe_2O_3 Sample 1 (black), Si/hollow Fe_2O_3 Sample 2 (red curve), and Si/Fe Sample 3 (blue curve): magnetic hysteresis loop M(H) at 2 K (A). Temperature dependence of the magnetization following a Zero-Field Cooled/Field Cooled procedure (B).

been followed by magnetic measurements (Figure S4). The process is complete after a month in ambient conditions.

The full characterization of the composite is consistent with the formation of pristine Sample 1: Si/Fe@γ-Fe_2O_3. An exposure to air yields Sample 2: Si/hollow γ-Fe_2O_3. An annealing step in forming gas yields Sample 3 (Si/Fe).

■ ELECTROCHEMISTRY

The materials have been tested as anode in coin cell with Li metal and an electrolyte solution of $LiPF_6$ 1 mol/L in fluoroethylene carbonate/dimethylcarbonate (FEC/DMC) 1:4 ratio. Cycling is performed at 1C (charge in 1 h and discharge in 1 h), at a controlled temperature of 30 °C. Only the electrochemistry of Si@hollow γ-Fe_2O_3 (Sample 2) is discussed in the following, while the electrochemical properties of other samples are reported in the Supporting Information.

Figure 6 presents the specific capacities measured for Si and Si@hollow γ-Fe_2O_3 composites for 50 cycles. All capacities are normalized to the mass of Si. Si nanopowder exhibits a state of the art reversible capacity of 2000 mAh/g_{Si}. Sample 2 Si@hollow γ-Fe_2O_3 displays a specific capacity of 2600 mAh/g_{Si}. Only Sample 2 displays higher specific capacity, while the other samples display lower specific capacity than the pristine Si sample (Figure S5). The origin of the high value obtained for the Si@hollow γ-Fe_2O_3 was investigated through electrochemical measurements. The samples display high Coulombic efficiency which reaches 98.8% after 50 cycles for the Sample 2 (Figure 6).

DOI: 10.1021/acs.chemmater.5b00730
Chem. Mater. 2015, 27, 2703−2710

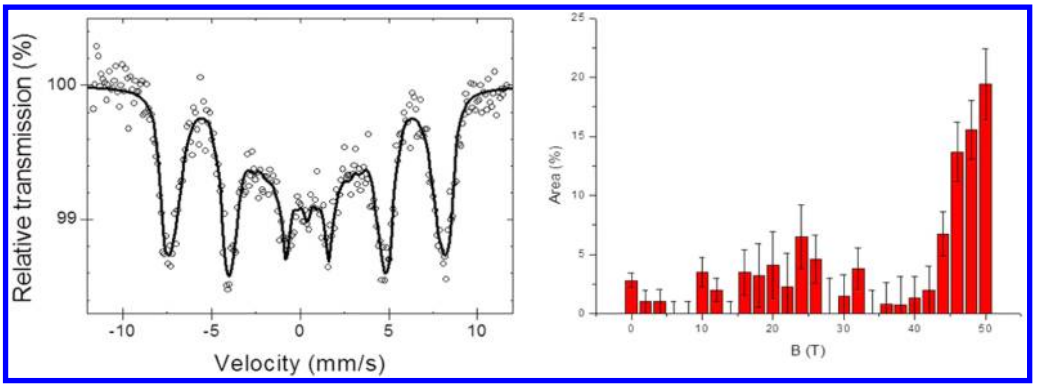

Figure 5. Mössbauer measurement at 4.2 K of Si/hollow Fe_2O_3 NCs (Sample 2) and corresponding magnetic hyperfine distribution.

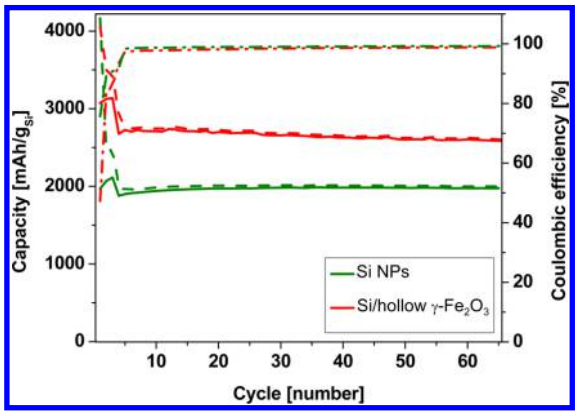

Figure 6. Galvanostatic cycling of the Li-ion half-cell with Si@hollow γ-Fe_2O_3 (Sample 2) as anode material (red curve) and pristine Si NPs (green curve). The dash curves are the charge measurements, the continuous curves are the discharge measurements, and the dash dot curves are the Coulombic efficiency.

The rate capability of the Si@hollow γ-Fe_2O_3 has been measured from C/5 up to 5C (Figure S6).

The electrodes of pristine Si display a typical cyclic voltammetry for silicon. We observe two lithiation plateaus at 0.16 and 0.025 V vs Li in discharge and delithiation at 0.33 and 0.52 V vs Li in charge (Figure 7A). These two events correspond to the formation of two main phases of Li_xSi alloys.[21] The first three cycles (Figure 7A) show increasing current density related to the high scanning rate applied during the cyclic voltammetry (1 mV/s), while the next 50 cycles (Figure 7C) show highly reversible processes. The cyclic voltammetry of the Si@hollow γ-Fe_2O_3 shows two marked reduction peaks at 1.4 and 0.8 V which are not present or very weak in the pure Si electrode (Figure 7B). Prolonged cycling of the electrode (Figure 7D) between 0 and 0.8 V shows the two features already observed with pristine Si without a noticeable change in the potential or intensity ratios between the peaks. The voltammetry displays only a vanishing shoulder at 0.4 V in reduction (Figure 7D).

The reduction peaks observed in the potential window {2.5−0.7 V} during the first lithiation do not contribute to a reversible insertion of Li and do not account for the higher specific capacity observed in galvanostatic measurements (Figure 6). These peaks are consistent with the insertion of Li in γ-Fe_2O_3 in a conversion reaction which finally yields metallic Fe. This reaction does not appear to be reversible in the potential window {0−1 V}.

As presented above, the reaction mechanism is difficult to investigate due to the amorphous nature of the iron compounds. The electrodes have been cycled, and ex situ magnetic measurements on the electrodes have been performed to validate our assumption of Fe(0) irreversible formation. The magnetic measurements are carried out directly on the electrode after disassembling the coin cell, removing the electrode and drying the electrode (Si@hollow γ-Fe_2O_3 on Cu foil). These experiments have been performed on other conversion materials to assess the mechanism, and in situ measurements have confirmed the results obtained by ex situ magnetism.[22]

The hysteresis loops show the diamagnetic contribution from Si but mainly the ferromagnetic contribution from Fe species at 2 K (Figure 8A). The magnetic moment plots correspond to the same electrode area. After full lithiation (0.01 V), the magnetic moment reaches a value 3 times higher than the pristine material, while after full delithiation, the magnetic moment relaxes to twice the value of the pristine material. Hollow γ-Fe_2O_3 displays a magnetic moment close to the bulk value (67 emu/g), and the fully lithiated compound displays a value that would then correspond to 200 emu/g (calculated from the ratio between the magnetic moments at 2T on Figure 8A). The high value is the clear signature for the formation of Fe after full lithiation. The delithiated compound shows a slight relaxation to a calculated value of 140 emu/g which accounts for the reminiscent metallic Fe with some surface passivation process.

Temperature dependence magnetism (Figure 8B) is characteristic of a superparamagnetic behavior with a ZFC peak close to 16 K which corresponds to smaller magnetic particles than the pristine material (13 nm hollow γ-Fe_2O_3) with an eventual drop in the magnetic anisotropy. At this point, the refinement on these two parameters (magnetic particle size and anisotropy) is too preliminary. A closer look at the hysteresis loop confirms qualitatively the nature of the phases observed. The coercive field drops from H_C = 100 mT (nonsymmetric) in the pristine sample to 50 mT in the lithiated or delithiated electrode which validates the formation of metallic Fe (a soft magnetic material).

A schematic representation of the nature of the electrode material at each stage of the cycling was presented in Figure 8C. γ-Fe_2O_3 was converted to Fe during the first lithiation and remains as metallic Fe during the Si delithiation. This picture is consistent with the potential window used for the cycling [0−0.8 V] which is lower than the oxidation potential of Fe. Therefore, the improved reversible specific capacity observed in the Si/hollow γ-Fe_2O_3 is not related to an additional conversion reaction of γ-Fe_2O_3 and can be fully attributed to a surface effect due to the interface with Fe and the byproducts formed during the first lithiation. Interestingly, this layer has to be formed in situ during the cycling, and the efforts to cycle previously reduced Fe (Sample 3 Si/Fe) do not show any enhancement of the specific capacity (Figure S5). Therefore, the improved electrochemical

DOI: 10.1021/acs.chemmater.5b00730
Chem. Mater. 2015, 27, 2703−2710

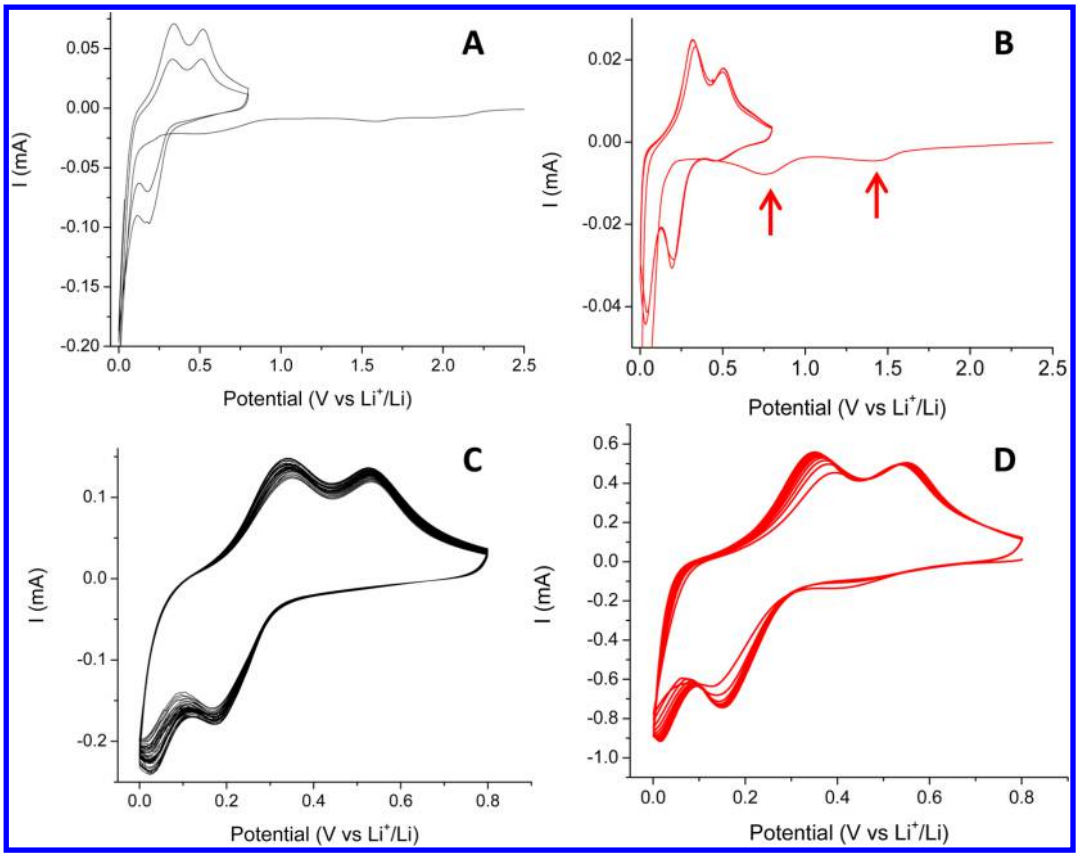

Figure 7. Cyclic voltammetry of pristine Si NPs (A,C) and Si/hollow Fe_2O_3 NPs (B,D). The upper panel (A,B) presents the first 3 cycles, while the lower panel presents the next 50 cycles (C,D).

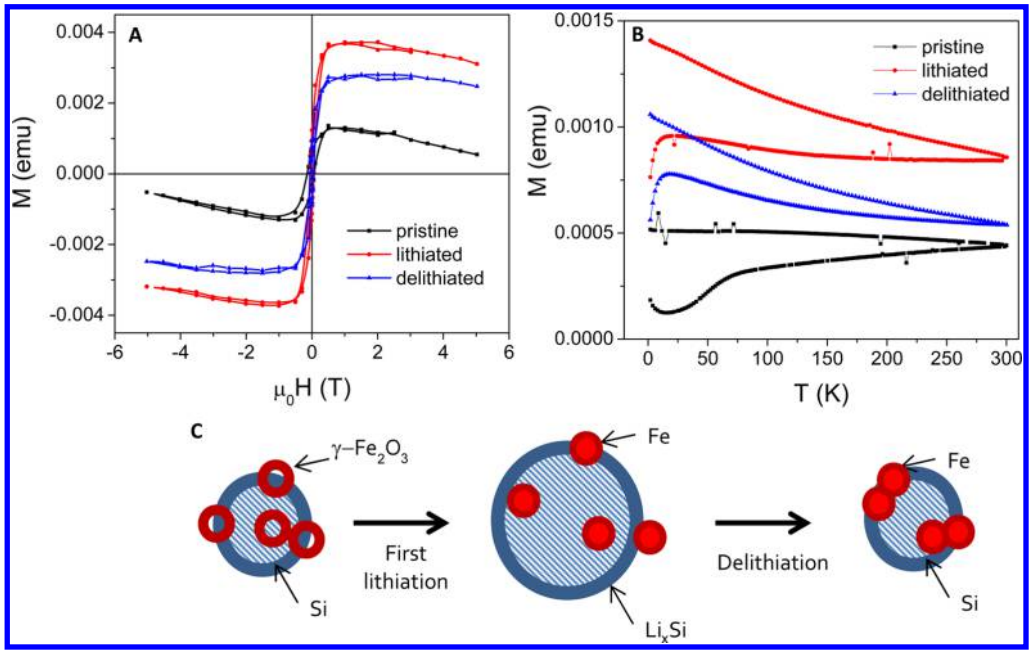

Figure 8. Magnetic measurements on electrodes before (black) and after cycling: full lithiation (red) and full delithiation (blue): hysteresis loops at 2 K (A) and temperature dependence ZFC/FC (B). Schema of the composite for each stage of the cycling (C).

results could be derived from the specific hollow shape of the γ-Fe_2O_3 nanoparticles.

Our results could be linked to the specific hollow morphology of the γ-Fe_2O_3 nanoparticles since this morphology has been found to be beneficial for enhancing specific capacity of γ-Fe_2O_3 itself as nanoparticles,[23] microparticles,[24] or porous amorphous networks.[25] Reports in the literature on γ-Fe_2O_3 have shown the benefits of hollow iron oxides nanoparticles for the electrochemical properties, mainly capacity and Coulombic efficiency. Switching to the investigation of Si/Fe composite in the

DOI: 10.1021/acs.chemmater.5b00730
Chem. Mater. 2015, 27, 2703−2710

literature, metallic Fe formed during lithiation of SiO/Fe_2O_3 micropowder has been pointed as the origin of an increasing conductivity of the composite and thereby significantly improved performance.[17] Similarly, a model system of Si/Fe multilayer film anodes has shown the stable cyclic performance and reversible cyclability with increasing thickness of the inactive Fe buffer layers.[26]

These layered structures, investigated as model compounds, are nevertheless far from the nanoparticles morphology investigated in this article. As demonstrated by TEM-EDS analysis, iron oxide is located on the surface of the particles and is converted to Fe (and presumably Li_2O) during the first lithiation (cyclic voltammetry on Figure 7 and magnetic measurements on Figure 8). The impact of this oxide layer should be detrimental to the conductivity, and such a relationship between specific capacity and electronic conductivity of the anode does not match the observation of decreased specific capacity in Si/metallic Fe Sample 3 (Figure S5). Therefore, the explanation of the enhanced capacity of Si with Fe_2O_3 modification cannot be understood in terms of electronic conductivity, and the observed enhancement could find its origin in the morphology and chemical nature of the SEI. Interestingly, a similar nanocomposite Si/α-Fe_2O_3 has been recently used as photoanode for water splitting and the influence of α-Fe_2O_3 thickness on the electronic interface with Si has been demonstrated.[27] Such an influence of the morphology of the iron oxide coating on the electronic properties of the Si interface should result in the formation of a thicker SEI. Indeed, the results on rate capability (Figure S6) also demonstrate the better kinetics for Si vs Si/γ-Fe_2O_3 at high rate (above 5C), while Si/γ-Fe_2O_3 shows much higher capacity at lower rates (below 1C). The latter results point out to the influence of the pretreatment of the Si for the formation of better SEI. The understanding of the origin of this phenomenon requires a full analysis of the surface chemistry of the anode materials during cycling.

■ CONCLUSIONS

Si/hollow γ-Fe_2O_3 has been synthesized through an organometallic route followed by a slow oxidation "Kirkendall" process. The electrochemical properties of the composite present an enhancement of more than 30% of the specific capacity of Si (2600 mAh/g_{Si}) compared with pristine Si. This high and stable specific capacity is observed only for the Si/hollow γ-Fe_2O_3 composite. The lithiation mechanism is typical of nanocrystalline Si except for the first lithiation which shows the conversion of γ-Fe_2O_3 to metallic Fe in the composite. The nature of the phases is clearly deduced from the magnetic measurements performed on the electrodes after cycling. The enhancement of specific capacity is believed to result from the hollow γ-Fe_2O_3 on the Si surface which may provide effective "channels" for the Li-ions toward the Si surface.

■ METHODS

Material. Silicon nanoparticles of sub-50 nm (nanopowder 98%, Sigma-Aldrich) were used as received. Iron pentacarbonyl $Fe(CO)_5$ (99.5%, ACROS) and ethanol absolute (extra dry 99.5%, Acros) were stored in a glovebox (N_2 filled, O_2 < 1 ppm, H_2O < 1 ppm). 1-Octadecene (ACROS, 90%) was dried, degassed, and stored on molecular sieves in the glovebox.

Synthesis of Sample 1 Si/Fe@γ-Fe_2O_3, Sample 2 Si/γ-Fe_2O_3, and Sample 2 Si/Fe Nanoparticles. Si nanopowder (0.082 g) was dispersed in 1-octadecene (3 mL), followed by the addition of $Fe(CO)_5$ (0.1 mL) in 1-octadecene (2 mL). The mixture was stirred at 280 °C for 2 h under N_2. The dispersion was centrifuged at 6000 rpm for 10 min to separate the dark brown solid and redispersed in dry ethanol. The procedure of washing was repeated three times to yield dry Sample 1 (Si/Fe@γ-Fe_2O_3). The stoichiometry was checked by ICP-AES.

The dark brown powder of Si/Fe@γ-Fe_2O_3 was used as the starting material for the formation of Si/γ-Fe_2O_3. A further exposure to air (one month in room environment) yielded Sample 2 (Si/γ-Fe_2O_3).

The dark brown powder of Si/Fe@γ-Fe_2O_3 was used as the starting material for the formation of Si/Fe by annealing the powder in forming gas. The reduction step was achieved by placing the dry sample 2 in a tubular furnace under forming gas (Ar/H_2 95/5, 99.999%). The sample was heated to 1000 °C using a 1 h ramp heating procedure and maintained at this temperature for 5 min, to yield Sample 3 (Si/Fe) nanocomposite. The as-prepared samples were rapidly transferred to a glovebox filled (Ar filled, O_2 < 1 ppm, H_2O < 1 ppm).

Characterization. The structure of the NPs is investigated by TEM:FEI Tecnai-12 at 120 kV and JEOL JEM-2100 (LaB6) at 200 kV for high resolution imaging (HR-TEM). Fourier transform analysis (FFT) of high-resolution images technique was used for structural analysis. HR-TEM images together with EDS were obtained by a JEOL JEM-2100F Field Emission Electron Microscope operated at 200 kV.

XPS analyses were performed in a Kratos AXIS-HS spectrometer, using a monochromatized Al K_α source. Scans were collected at 150 W with detection pass energies of 80 and 40 eV, respectively, for low and high resolution scans. All XPS measurements were carried out at room temperature, under high vacuum ($<3.0 \times 10^{-9}$ Torr). Data processing was done with VISION 2.1 software ("Kratos"), and Vision 2.1 sensitivity factors were used for quantification.

^{57}Fe Mössbauer spectrum was measured with a source of ^{57}Co in rhodium metal. The measurements were performed with the absorber at 4.2 K. In all experiments the ^{57}Co source was always kept at ambient temperature (294 K).The spectrometer was operated with a triangular velocity waveform, and a NaI scintillation detector was used for the detection of the γ rays. The spectra was fitted with a distribution of Lorentzian lines using the PC-Mos II computer program. The spectral parameters such as the isomer shift (δ), the electric quadrupole shift (ε), and the full line width at half-maximum (Γ_{exp}) were kept identical to all the components of distribution. Only the magnetic hyperfine field (B) and the relative resonance areas (A) of the different components were free (distribution of B).

Magnetic properties were measured using a SQUID magnetometer MPMS XL7, in the range of temperature 2−300 K and of field 0−5 T. The temperature-dependent susceptibility was measured using DC procedure. The samples were cooled to 2 K under zero magnetic field, low magnetic field (5.0 mT) was applied, and data were collected from 2 to 300 K (zero-field cooled, ZFC). Field Cooled (FC) measurements were performed from 2 to 300 K with an applied field during the cooling. Hysteresis loop was measured at 2 K.

Electrochemistry. All work was conducted in an argon filled glovebox. Electrode materials (Si, Si/Fe@γ-Fe_2O_3, Si/γ-Fe_2O_3 and Si/Fe) were laminated onto a roughened copper foil (Oxygenfree, SE-Cu58, Schlenk Metallfolien GmbH & Co. KG). Silicon powder was equally spread on the surface, and adhesion to the current collector was enhanced by applying manual pressure with a Kimwipes paper (Figure 1B).

Anodes were tested in coin-type cells (2523, NRC, Canada) vs lithium metal (Chemetall Foote Corporation, USA). Electrolyte solution was fluoroethylene carbonate FEC (Aldrich, < 20 ppm water) and dimethyl carbonate DMC (Aldrich, < 20 ppm water) (1:4 ratio) with 1 M $LiPF_6$ (Aldrich). The cells were assembled in an argon-filled glovebox, with a purifying system (MBraun GmbH, Germany), oxygen, and water contents below 1 ppm.

Cyclic voltammetry was measured with Bio-Logic VMP3, multichannel potentiostat at 1 mV/s between 0.8 and 0.0 V vs Li+/Li which accounts for a charge and discharge duration of 800 s. Coin-cells were cycled at 30 °C using BT2000 battery cycler (Arbin Instruments, USA) (first discharge: C/20, two cycles: C/10, therefore C rate: all capacity in 1 h). The active mass of silicon anodes was measured on an analytical balance and confirmed by dissolving silicon and dosing with ICP-AES.

DOI: 10.1021/acs.chemmater.5b00730
Chem. Mater. 2015, 27, 2703−2710

■ ASSOCIATED CONTENT

Supporting Information

Figures S1−S6. This material is available free of charge via the Internet at http://pubs.acs.org.

■ AUTHOR INFORMATION

Corresponding Author

*E-mail: David.Zitoun@biu.ac.il.

Notes

The authors declare no competing financial interest.

■ ACKNOWLEDGMENTS

The authors thank M. T. Sougrati for the ^{57}Fe Mössbauer spectroscopy measurements and analysis, Dr. Y. Grinblat and Dr. V. Ezersky for carrying out the HR-TEM and EDS measurements, and Y. Goffer for the XPS study. This work was supported by the High Council for Scientific and Technological Cooperation between France-Israel (3-8675) and the I-CORE program of the planning and budgeting committee and the Israel Science Foundation (2797/11).

■ REFERENCES

(1) Kasavajjula, U.; Wang, C.; Appleby, A. *J. Power Sources* **2007**, *163*, 1003−1039.

(2) Chan, C. K.; Peng, H.; Liu, G.; McIlwrath, K.; Zhang, X. F.; Huggins, R. A.; Cui, Y. *Nat. Nanotechnol.* **2008**, *3*, 31−5.

(3) Fournier, C.; Favier, F. *Electrochem. Commun.* **2011**, *13*, 1252−1255.

(4) Teki, R.; Datta, M. K.; Krishnan, R.; Parker, T. C.; Lu, T.-M.; Kumta, P. N.; Koratkar, N. *Small* **2009**, *5*, 2236−42.

(5) Lee, Y. M.; Lee, J. Y.; Shim, H.-T.; Lee, J. K.; Park, J.-K. *J. Electrochem. Soc.* **2007**, *154*, A515.

(6) Xu, W.; Vegunta, S. S. S.; Flake, J. C. *J. Power Sources* **2011**, *196*, 8583−8589.

(7) Elazari, R.; Salitra, G.; Gershinsky, G.; Garsuch, A.; Panchenko, A.; Aurbach, D. *Electrochem. Commun.* **2012**, *14*, 21−24.

(8) Cui, L.-F.; Hu, L.; Wu, H.; Choi, J. W.; Cui, Y. *J. Electrochem. Soc.* **2011**, *158*, A592.

(9) Markevich, E.; Fridman, K.; Sharabi, R.; Elazari, R.; Salitra, G.; Gottlieb, H. E.; Gershinsky, G.; et al. *J. Electrochem. Soc.* **2013**, *160*, A1824−A1833.

(10) Corathers, L. A. *Miner. Yearb.* **2009**, 67.

(11) Ge, M.; Lu, Y.; Ercius, P.; Rong, J.; Fang, X.; Mecklenburg, M.; Zhou, C. *Nano Lett.* **2014**, *14*, 261−268.

(12) Koltypin, M.; Aurbach, D.; Nazar, L.; Ellis, B. *Electrochem. Solid-State Lett.* **2007**, *10*, A40.

(13) Yamada, A.; Chung, S. C.; Hinokuma, K. *J. Electrochem.* **2001**, 500.

(14) Chernova, N. A.; Nolis, G. M.; Omenya, F. O.; Zhou, H.; Li, Z.; Whittingham, M. S. *J. Mater. Chem.* **2011**, *21*, 9865−9875.

(15) Zhang, X.; Ohara, S.; Okawa, H.; Maric, R.; Fukui, T. *Solid State Ionics* **2001**, *139*, 145−152.

(16) Larcher, D.; Masquelier, C.; Bonnin, D.; Chabre, Y.; Masson, V.; Leriche, J.-B.; Tarascon, J.-M. *J. Electrochem. Soc.* **2003**, *150*, A133−A139.

(17) Zhou, M.; Gordin, M. L.; Chen, S.; Xu, T.; Song, J.; Lv, D.; Wang, D. *Electrochem. Commun.* **2013**, *28*, 79−82.

(18) Bridel, J.-S.; Azaïs, T.; Morcrette, M.; Tarascon, J.-M.; Larcher, D. *Chem. Mater.* **2010**, *22*, 1229−1241.

(19) Khurshid, H.; Li, W.; Phan, M.-H.; Mukherjee, P.; Hadjipanayis, G. C.; Srikanth, H. *Appl. Phys. Lett.* **2012**, *101*, 022403.

(20) Hung, L.-I.; Tsung, C.-K.; Huang, W.; Yang, P. *Adv. Mater.* **2010**, *22*, 1910−1914.

(21) Wilson, A. M.; Zank, G.; Eguchi, K.; Xing, W.; Dahn, J. R. *J. Power Sources* **1997**, *68*, 195−200.

(22) Gershinsky, G.; Bar, E.; Monconduit, L.; Zitoun, D. *Energy Environ. Sci.* **2014**, *7*, 2012.

(23) Koo, B.; Xiong, H.; Slater, M. D.; Prakapenka, V. B.; Balasubramanian, M.; Podsiadlo, P.; Johnson, C. S.; Rajh, T.; Shevchenko, E. V. *Nano Lett.* **2012**, *12*, 2429−35.

(24) Xu, S.; Hessel, C. M.; Ren, H.; Yu, R.; Jin, Q.; Yang, M.; Zhao, H.; Wang, D. *Energy Environ. Sci.* **2014**, *7*, 632.

(25) Jiang, Y.; Zhang, D.; Li, Y.; Yuan, T.; Bahlawane, N.; Liang, C.; Sun, W.; Lu, Y.; Yan, M. *Nano Energy* **2014**, *4*, 23−30.

(26) Kang, H.-K.; Lee, S.-R.; Cho, W. I.; Cho, B. W. *Phys. Chem. Chem. Phys.* **2013**, *15*, 1569.

(27) Qi, X.; She, G.; Huang, X.; Zhang, T.; Wang, H.; Mu, L.; Shi, W. *Nanoscale* **2014**, *6*, 3182−3189.

DOI: 10.1021/acs.chemmater.5b00730
Chem. Mater. 2015, 27, 2703−2710